CHAPTER 5 NUMERICAL MODELING OF A NON-SPRAYED POROUS BURNER (NSPB)

Liquid fuel is popularly used in industrials application because it has higher energy contents per unit volume than gases. It is also easier to storage and distribute than solid fuel. In the other word, liquid fuel offers the best combination of energy content and safety to use. The previous works were dealt with droplet evaporation in the free space and the liquid atomizers were used. Moreover, the combustion of liquid fuel sprayed was a heterogeneous combustion, which is emitted more emission as compare with a homogeneous combustion.

Present in this chapter is a new concept of non-sprayed porous burner (NSPB) for liquid kerosene by mean of numerical modeling. The emphatic of NSPB are to reduce complexity of atomization process by using a porous evaporator (FP). Beside homogeneous combustion within a porous combustor (PC) is used instead of a heterogeneous combustion in a free space of conventional sprayed burner. The combustion occur in NSPB is late mixing combustion. Thus, fuel and air can be preheated without auto-ignition outside the porous combustion. Furthermore, air preheating can be avoided condensation of vapor kerosene in a mixing chamber. The local thermal non-equilibrium between fluid and solid phase with phase change, one-dimensional, steady state approach, and single-step global reaction are considered. Subcooled boiling of the isothermal thin film of saturated liquid at 250 ^{o}C within a small evaporation volume is assumed.

The evaporation and combustion phenomena of NSPB are investigated. The evaporation front and reaction zone cannot be indicated by an experimental study; hence the limitations can be overcome by numerical model of NSPB. Firstly, the numerical model of NSPB has been validated with the experimental data. The main influential parameter inclusive of equivalence ratio, firing rate, and porous combustor type was investigated in order to identify the burner performance in term of radiant output efficiency. The results shown that, the self-sustaining evaporation without atomization and matrix stabilized flame can be achieved with the NSPB use is enhanced the radiant output efficiency in the same range as a conventional

premixed porous burner. Therefore, the NSPB is an alternative technology, which will be suggested as a replace for the conventional spray burners to future requirement.

5.1 Numerical model

5.1.1 Burner geometry

Previous chapter, the results indicated that operating in case of preheated air provide highest preheat and radiant output efficiency. Therefore, in this chapter, only the numerical modeling in case of preheated is studied.

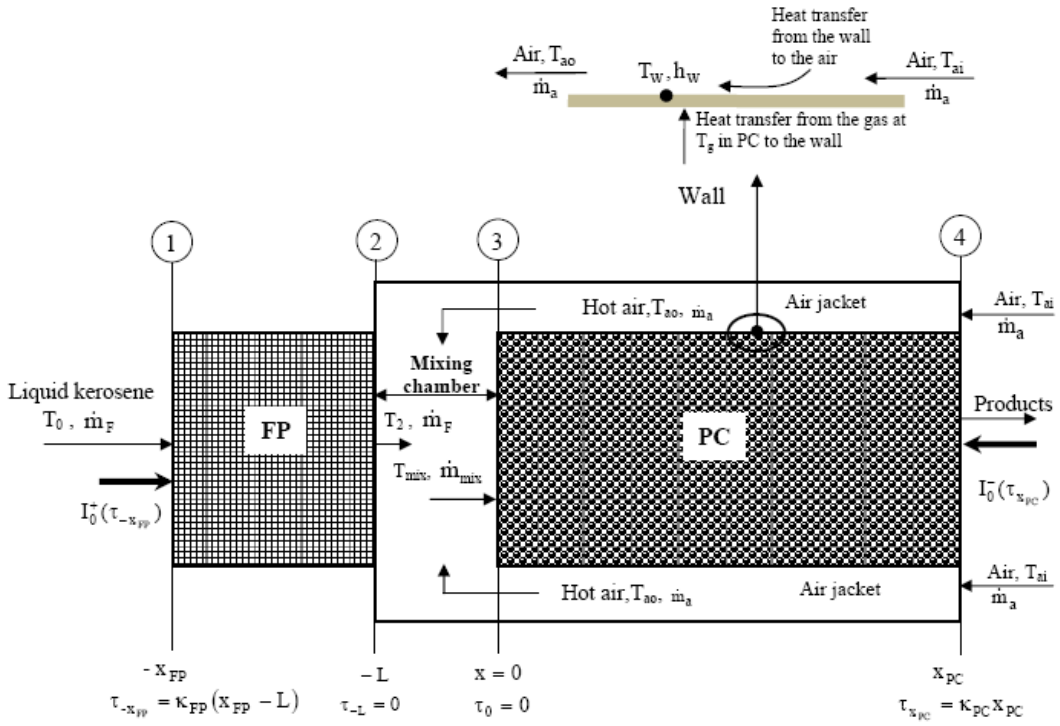

Figure 5.1 Burner geometry.

Fig.5.1 shows non-premixed without spray porous burner using liquid kerosene geometry. The burner consists of two major steps as follows: a fuel-preheated porous medium (FP) and a porous combustor (PC), which is surrounded by an air jacket. The fuel and air supplies are separated for safety reasons. The liquid fuel at T_0 flows into the FP at section 1, the liquid fuel was preheated by the hot porous

matrix of FP. When the liquid temperature reaches T_b, the liquid phase is completely evaporated and changed to gas phase. The vapor fuel is also preheated by porous media before the superheated vapor fuel flow out from FP at section 2. At the same time, the combustion air with inlet temperature T_{ai} flows through and preheated via an annular air jacket at section 4. The superheated vapor fuel and the hot air from section 2 of FP and section 3 of the air jacket, respectively, have been flown and mixed in the mixing chamber and combustion later within the PC. The total length of the burner is 260 mm (FP section is 80 mm length, mixing chamber is 20 mm length, and the PC section is 160 mm length). The computation domain is discretized into 200 grid points (100 grid points for FP and 100 grid points for PC). Both ends of the NSPB are exposed to black surroundings maintained at ambient temperature T_0 providing incident radiation $I_0^+\left(\tau_{-x_{FP}}\right)$ at section 1 and $I_0^-\left(\tau_{x_{PC}}\right)$ at section 4, respectively.

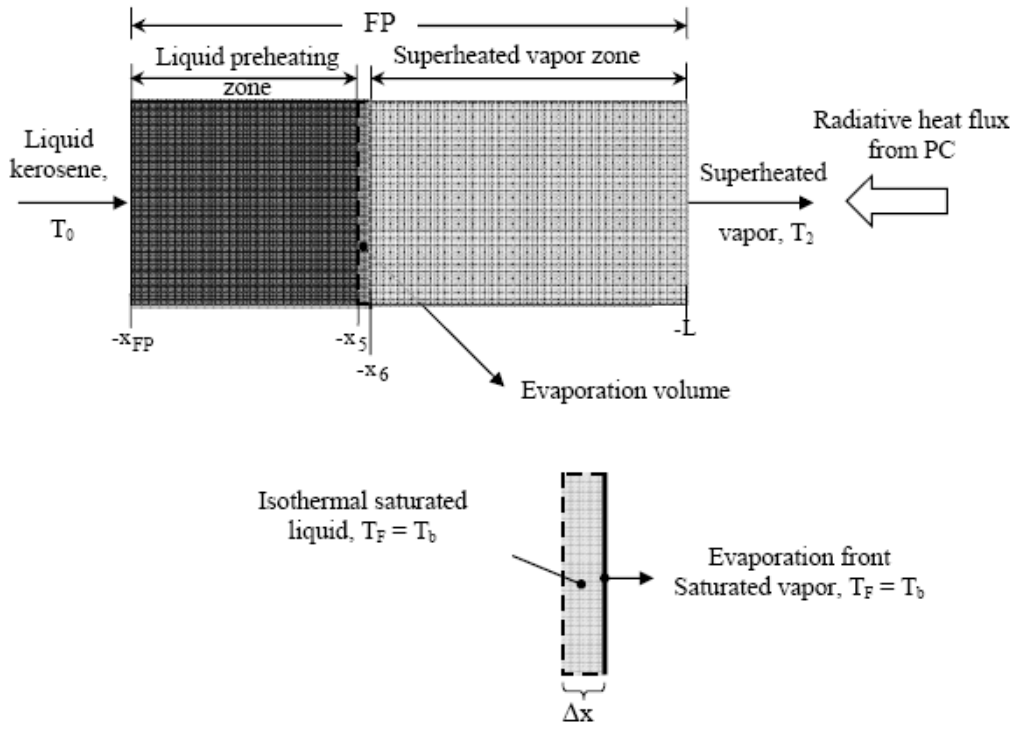

Figure 5.2 Evaporation model.

Fig.5.2 shows magnification of the FP section at liquid preheated zone in FP, when the liquid fuel temperature reaches T_b, the fuel is in saturated liquid state. The fuel is then assumed to be an isothermal thin film at T_b within a small control volume,

which has the thickness of 8×10^{-4} m. The flash evaporation process occurs at an exit of this volume (i.e., evaporation front). At the evaporation front, the fuel immediately changes from saturated liquid to saturated vapor at T_b and the fuel density significantly increase due to the phase change. This causes to increase the flow velocity. In addition, the higher vapor flow velocity compare with the liquid, whereas the mass flow rate is still conserved. Then, the vapor fuel gets preheated and their temperatures rise in the superheated vapor zone. The evaporation process in this model is namely "isothermal thin film flash evaporation".

The principal assumptions, which are presented in section 5.1.2, are performed in order to simplify the complicated phenomena of evaporation and combustion under complex heat transfer in porous media.

5.1.2 Principal assumptions

The principal assumptions are used in the model are already elucidated in section 4.1.2 so only the additional assumptions are considered in the evaporation model are presented:

(a) At steady state condition, the PC emits thermal radiation to FP for preheating and evaporation process.

(b) The fuel flow velocity and the direction of thermal radiation from the PC to the FP are counter. The feeding liquid kerosene is gradually preheated until its temperature reaches its boiling point thus the evaporation process is considered to be a sub-cooled boiling at saturation temperature.

(c) The boiling temperature of kerosene is assumed constant at $T_b = 250\ ^oC$. The flash evaporation process occurs only in a small control volume in FP and the temperature of fluid in this volume is constant and equal to the boiling temperature, T_b of kerosene.

(d) The evaporation process in FP is occurred under relatively small mass flow rate of liquid fuel. The latent heat of kerosene is very small when compared to

thermal radiation energy emitted from PC. Therefore, the evaporation rate is assumed equal to the fuel mass flow rate.

(e) At the liquid preheating zone in the FP, the kerosene is in sub-cooled liquid state, further the fuel is considered vapor state.

(f) The evaporation front is considered moving boundary at which the liquid and vaporized kerosene are separated.

5.1.3 Basic equations

The governing equations are as follows.

In the FP section, $-x_{FP} \le x \le -L \ \left(\tau_{-x_{FP}} \le \tau \le \tau_{-L}\right)$,

the conservation equation for energy of solid phase is given by

$$\rho_s c_s (1-\varepsilon)\frac{\partial T_s}{\partial t} = \lambda_e \frac{\partial^2 T_s}{\partial x^2} - \frac{\partial q_r^n}{\partial x} - h_v (T_s - T_F) \ . \qquad (5.1)$$

Where the local net radiative heat flux within the FP is expressed as:

$$q_r{}^n(\tau) = q_r{}^+(\tau) + q_r{}^-(\tau),$$

$$q_r{}^+(\tau) = 2\pi\left[I_0^+(\tau_{-x_{FP}}) E_3\left(\tau_{-x_{FP}} - \tau\right) + \int_{\tau_{-x_{FP}}}^{\tau} I_b(\tau') E_2(\tau' - \tau) d\tau \right], \quad \text{and} \qquad (5.2)$$

$$q_r{}^-(\tau) = -2\pi\left[I_0^-(\tau_{x_{PC}}) E_3\left(\tau_{x_{PC}}\right) + \int_0^{\tau_{x_{PC}}} I_b(\tau') E_2(\tau') d\tau' \right] E_3(\tau) - 2\pi\left[\int_{\tau}^{\tau_{-L}} I_b(\tau') E_2(\tau - \tau') d\tau' \right] . \qquad (5.3)$$

The optical thickness in the FP section $\left(\tau_{-x_{FP}} \le \tau \le \tau_{-L}\right)$ is defined as $\tau = \kappa_{FP}\left(-L - x\right)$. The divergence of net radiative heat flux, $\frac{\partial q_r^n(\tau)}{\partial x}$ in equation (5.1), is evaluated from the integration of the radiant flux from each part of the porous medium, and is expressed as:

$$\frac{\partial q_r^n(\tau)}{\partial x} = -2\kappa_{FP}\pi\left[-2I_b(\tau) + \int_{\tau_{-x_{FP}}}^{\tau_{-L}} I_b(\tau')E_1\left(\left|\tau-\tau'\right|\right)d\tau' + I_0^+\left(\tau_{-x_{FP}}\right)E_2\left(\tau_{-x_{FP}}-\tau\right)\right]$$
$$-2\kappa_{FP}\pi\left[I_0^-\left(\tau_{x_{PC}}\right)E_3\left(\tau_{x_{PC}}\right) + \int_0^{\tau_{x_{PC}}} I_b(\tau')E_2(\tau')d\tau'\right]E_2(\tau)$$
$$-2\kappa_{PC}\pi\left[I_0^-\left(\tau_{x_{PC}}\right)E_2\left(\tau_{x_{PC}}\right) + I_b(\tau') + \int_0^{\tau_{x_{PC}}} I_b(\tau')E_1(\tau')d\tau'\right]E_3(\tau)\ . \tag{5.4}$$

Where $I_b(\tau) = \frac{\sigma T_s^4(\tau)}{\pi}$,

$$\int_{\tau_{-x_{FP}}}^{\tau_{-L}} I_b(\tau')E_1\left(\left|\tau-\tau'\right|\right)d\tau' = \int_{\tau_{-x_{FP}}}^{\tau} I_b(\tau')E_1(\tau'-\tau)d\tau' + \int_{\tau}^{\tau_{-L}} I_b(\tau')E_1(\tau-\tau')d\tau'$$

and $E_n(\tau) = \int_0^1 \eta^{n-2}\exp(-\tau/\eta)d\eta$, $\quad n = 1, 2, 3.$

The energy equation for fuel is considered both in liquid preheated zone $\left(-x_{FP} \le x \le -x_5\right)$ and superheated vapor zone $\left(-x_6 \le x \le -x_L\right)$, is given by

$$\rho_F c_F \varepsilon \frac{\partial T_F}{\partial t} + \rho_F u_F c_F \varepsilon \frac{\partial T_F}{\partial x} = \lambda_F \varepsilon \frac{\partial^2 T_F}{\partial x^2} + h_v(T_s - T_F) \tag{5.5}$$

The subscript F in equation (5.5) means liquid phase (liquid preheated zone) and gas phase (superheated vapor zone). In evaporation volume (Fig.5.2), the fuel is in isothermal equilibrium at boiling temperature T_b. The convection and conduction heat transfer of saturated fuel are neglect. Thus, the latent heat of evaporation is equal to heat transfer from hot solid to saturated liquid. The considered equations for this volume are given by

$$T_F = T_b, \text{ and} \tag{5.6}$$

$$q_L = h_v(T_s - T_b). \tag{5.7}$$

Where q_L = latent heat of evaporation per unit volume, $(W/m^3) = \frac{h_L \dot{m}_F}{V}$,

h_L = latent heat of kerosene (J/kg), and

V = evaporation volume (m^3) is shown in Fig. 5.2 $= \pi r_{FP}^2 \Delta x$.

$\dot{m}_F$ = fuel mass flow rate (kg/s)

In the mixing chamber, the conservation equations for mass and energy are given by

$$\dot{m}_{mix} = \dot{m}_F + \dot{m}_a, \text{ and} \tag{5.8}$$

$$\dot{m}_{mix} h_{mix}(T_{mix}) = \dot{m}_F h_F(T_2) + \dot{m}_a h_a(T_{ao}) . \tag{5.9}$$

In the PC section, $0 \le x \le x_{PC}$ $\left(\tau_0 \le \tau \le \tau_{x_{PC}}\right)$

The conservation equation for energy of gas phase in PC is given by

$$\rho_g c_g \varepsilon \frac{\partial T_g}{\partial t} + \rho_g u_g c_g \varepsilon \frac{\partial T_g}{\partial x} = \lambda_g \varepsilon \frac{\partial^2 T_g}{\partial x^2} + \varepsilon h_o w - h_v(T_g - T_s) - \alpha U_w(T_g - T_w). \tag{5.10}$$

The last term on the right-hand side of equation (5.10) is heat transfer from the hot gas in PC to the wall, which preheats the air flowing in the air jacket (Fig. 5.1). The reaction rate is considered to follow the first-order Arrhenius equation,

$$w = A\rho(1-y)\exp(-E/RT). \tag{5.11}$$

The conservation equation for the species of gas phase in PC is given by

$$\rho_g \varepsilon \frac{\partial y}{\partial t} + \rho_g u_g \varepsilon \frac{\partial y}{\partial x} = D\rho_g \varepsilon \frac{\partial^2 y}{\partial x^2} + \varepsilon w \,. \tag{5.12}$$

The conservation equation for the energy of solid phase in PC is given by

$$\rho_s c_s (1-\varepsilon)\frac{\partial T_s}{\partial t} = \lambda_e \frac{\partial^2 T_s}{\partial x^2} - \frac{\partial q_r^n}{\partial x} + h_v (T_g - T_s) \,. \tag{5.13}$$

Where the local net radiative heat flux within the PC is expressed as:

$$q_r^{\,n}(\tau) = q_r^{\,+}(\tau) + q_r^{\,-}(\tau),$$

$$\begin{aligned} q_r^{\,+}(\tau) = 2\pi & \left[I_0^+(\tau_{-x_{FP}}) E_3\left(\tau_{-x_{FP}}\right) + \int_{\tau_{-x_{FP}}}^{\tau_{-L}} I_b(\tau') E_2(\tau')\, d\tau' \right] E_3(\tau) \\ & + 2\pi \left[\int_0^{\tau} I_b(\tau') E_2(\tau - \tau')\, d\tau' \right] \end{aligned}, \tag{5.14}$$

and $$q_r^{\,-}(\tau) = -2\pi \left[I_0^-(\tau_{x_{PC}}) E_3(\tau_{x_{PC}} - \tau) + \int_{\tau}^{\tau_{x_{PC}}} I_b(\tau') E_2(\tau' - \tau)\, d\tau' \right] . \tag{5.15}$$

In PC section $(\tau_0 \le \tau \le \tau_{x_{PC}})$, the optical thickness is defined as $\tau = \kappa_{PC}(x)$ and the divergence of the net radiative heat flux, $\frac{\partial q_r^n(\tau)}{\partial x}$ in equation (5.13), is expressed as:

$$\frac{\partial q_r^n(\tau)}{\partial x} = -2\pi\kappa_{PC}\left[I_0^+\left(\tau_{-x_{FP}}\right)E_3\left(\tau_{-x_{FP}}\right) + \int_{\tau_{-x_{FP}}}^{\tau_{-L}} I_b(\tau')E_2(\tau')d\tau'\right]E_2(\tau)$$
$$-2\pi\kappa_{PC}\left[-2I_b(\tau) + I_0^-\left(\tau_{x_{PC}}\right)E_2\left(\tau_{x_{PC}} - \tau\right) + \int_0^{\tau_{x_{PC}}} I_b(\tau')E_1\left(\left|\tau - \tau'\right|\right)d\tau'\right] \quad (5.16)$$
$$-2\pi\kappa_{FP}\left[I_0^+\left(\tau_{-x_{FP}}\right)E_2\left(\tau_{-x_{FP}}\right) + I_b(\tau') + \int_{\tau_{-x_{FP}}}^{\tau_{-L}} I_b(\tau')E_1(\tau')d\tau'\right]E_3(\tau)\ .$$

Where $\int_0^{\tau_{x_{PC}}} I_b(\tau')E_1\left(\left|\tau - \tau'\right|\right)d\tau' = \int_0^{\tau} I_b(\tau')E_1(\tau - \tau')d\tau' + \int_{\tau}^{\tau_{x_{PC}}} I_b(\tau')E_1(\tau' - \tau)d\tau'$.

There are nine unknowns, T_F and T_s in the FP: $\dot{m}_{mix}$, T_{mix} and T_{ao} in the mixing chamber, T_g, T_s, y and T_w in the PC, but there are seven equations to be solved. Thus, another two equations are needed in the air jacket, which are shown in equations (5.17) and (5.18).

In the air jacket (see Fig. 5.1), heat transfer from the hot gas in PC to the wall is equal to heat convection from the wall to the combustion air in the air jacket, which in turn is equal to an increase in the sensible heat of the combustion air flowing in the air jacket. Therefore, we obtain

$$\int_0^{x_{PC}} U_w\left(T_g - T_w\right)\left(2\pi r_{PC}\right)dx = h_w A_w \Delta T_{ln}\,, \quad (5.17)$$

$$\dot{m}_a c_a dT_a = h_w\left(T_w - T_a\right)dA\,, \quad (5.18)$$

where $\Delta T_{ln} = \dfrac{\Delta T_o - \Delta T_i}{\ln\left(\Delta T_o / \Delta T_i\right)}$, $\Delta T_o = T_w - T_{ao}$, $\Delta T_i = T_w - T_{ai}$ and $T_{ai} = T_0$.

T_{ao}, in terms of T_w and T_{ai} is determined by integrating equation (5.18) over the surface area of the wall. By substituting T_{ao} into equation (5.17) gives the following

equation, $T_w = \dfrac{C\int_0^{x_{PC}} T_g(x)dx + (B-1)T_{ai}}{D}$, where B, C, and D are defined as $B = \exp(-2\pi r_{PC} x_{PC} h_w / \dot{m}_a c_a)$, $C = 2\pi r_{PC} U_w \ln B/(h_w A_w)$ and $D = C + Bx_{PC} - 1$.

In FP, the liquid flow velocity in the liquid preheating zone is small compared with the vapor in the superheated vapor zone, the heat transfer between the liquid and solid phases have no significantly changed with varying firing rates. Thus, the volumetric heat transfer in liquid preheating zone is considered constant and is equal to 9.1×10^5 W/m^3·K (Yoshizawa et al. 1988). The correlation for volumetric heat transfer coefficient Nu_v used in superheated vapor zone is given by the following correlation (Handley and Heggs 1968)

$$Nu_v = h_v d_p^2 / \lambda_g = (0.255/\varepsilon)(Pr^{1/3} Re_{d_P}^{2/3}) \qquad (5.19)$$

The correlation is used in PC is shown (Wakao et al. 1979):

$$Nu_v = h_v d_p^2 / \lambda_g = A_{sf} d_P (2 + 1.1 Re_{d_P}^{0.6} Pr^{1/3}). \qquad (5.20)$$

Where, the specific surface area is defined as $A_{sf} = \dfrac{6(1-\varepsilon)}{d_P}$.

The continuous porous structure is assumed and the effective conductivity of porous is $\lambda_e = (1-\varepsilon)\lambda_s$. The conservation equations of species and energy both in FP and PC are discretized by finite differential approximations. An implicit difference scheme is adopted with respect to time, and a central difference scheme is adopted with respect to space. The convergence criteria for numerical computation of all variables are set to 10^{-6}. Time step and mesh size were tested using different value. As a compromise between an accuracy and computational time, 100 uniform grid points both in the FP and PC, and 0.1 s time steps are selected. The final error in the energy balance is usually less than 1%. The boundary conditions are shown in table 5.1.

The gas's physical properties in this the model based on the average measured temperature at each zone, are constant. The physical properties of liquid in FP section are considered constant base on inlet temperature. All the porous properties used are summarized in Table 5.2. The experimental data are used for initial conditions.

Table 5.1 Boundary conditions.

FP Section		PC Section	
$x = -x_{FP}$	$x = -L$	$x = 0$	$x = x_{PC}$
$T_F = T_0$	$\frac{\partial T_F}{\partial x} = 0$	$T_g = T_{mix}$	$\frac{\partial T_g}{\partial x} = 0$
$\frac{\partial T_s}{\partial x} = 0$	$\frac{\partial T_s}{\partial x} = 0$	$\frac{\partial T_s}{\partial x} = 0$	$\frac{\partial T_s}{\partial x} = 0$
-	-	$y = y_0$	$\frac{\partial y}{\partial x} = 0$
$I_0^+(\tau_{-x_{FP}}) = \frac{\sigma T_0^4}{\pi}$	$I^-(\tau_{-L}) = I_0^-(\tau_{x_{PC}})E_3(\tau_{x_{PC}}) + \int_0^{\tau_{x_{PC}}} I_b(\tau')E_2(\tau')d\tau'$	$I^+(\tau_0) = I_0^+(\tau_{-x_{FP}})E_3(\tau_{-x_{FP}}) + \int_{\tau_{-x_{FP}}}^{\tau_{-L}} I_b(\tau')E_2(\tau')d\tau'$	$I_0^-(\tau_{x_{PC}}) = \frac{\sigma T_0^4}{\pi}$

Table 5.2 Solid property data used for simulations.

Properties	**FP**	**PC**	**Unit**
Porosity, ε	0.61	0.36	-
Effective thermal conductivity of solid, λ_e	12.1	1.8	$W.m^{-1}.K$
Volumetric heat transfer coefficient, h_v	Yoshizawa et al. 1988	Wakao et al. 1979	$W.m^{-3}.K$
Absorption coefficient, κ	1750	71	m^{-1}
Apparent density, $\rho_s(1-\varepsilon)$	2510	1714	kg/m^3
Specific heat, c_s	3120	775	$J.kg^{-1}.K^{-1}$

5.2 Solution procedures

The conservation equations of species and energy are transformed into dimensionless form. The dimensionless forms are approximated by finite difference expressions. Fixing a mass flow rate both in FP and PC are considered. An implicit difference scheme is adopted with respect to time, and a central difference scheme is adopted with respect to space. In FP, T_F and T_s are calculated, while in PC, $\dot{m}_{mix}$, T_{mix}, T_g, T_s,y, T_{ao}, and T_w are solved. The dimensionless terms using in this model, are as follows.

In the FP section, $-x_{FP} \le x \le -L \ \left(\tau_{-x_{FP}} \le \tau \le \tau_{-L}\right)$,

$$Re_{FP} = \frac{\rho_F u x_{FP}}{\mu_F},\ CD = (1-\varepsilon)\frac{\rho_F u x_{FP}}{\mu_F},\ \Gamma = \frac{\rho_s c_s}{\rho_F c_F},\ Pr = \frac{\mu_F c_F}{\lambda_F},\ Mp = \frac{h_v x_{FP}^2}{\lambda_F},$$

$$\tau_{FP} = \kappa_{FP} x_{FP},\ Nr = \frac{\kappa_{FP}\lambda_F}{4\sigma T_0^3},\ Le = \frac{\lambda_F}{D\rho_F c_F},\ X = \frac{x}{x_{FP}},\ \theta_F = \frac{T_F}{T_0},\ \theta_s = \frac{T_s}{T_0},\ H = \frac{q_r}{4\sigma T_0^4},$$

$$S = \frac{ut}{X_{FP}},\ J = \frac{\pi I}{\sigma T_s^4}$$

In the PC section, $0 \le x \le x_{PC} \ \left(\tau_0 \le \tau \le \tau_{x_{PC}}\right)$,

$$Re_{PC} = \frac{\rho_g u x_{PC}}{\mu_g},\ CD = (1-\varepsilon)\frac{\rho_g u x_{PC}}{\mu_g},\ \Gamma = \frac{\rho_s c_s}{\rho_g c_g},\ Pr = \frac{\mu_g c_g}{\lambda_g},\ Mp = \frac{h_v x_{PC}^2}{\lambda_g},$$

$$\tau_{PC} = \kappa_{PC} x_{PC},\ Nr = \frac{\kappa_{PC}\lambda_g}{4\sigma T_0^3},\ Le = \frac{\lambda_g}{D\rho_g c_g},\ Rs = \frac{x_{PC}^2 \rho_g A}{\mu_g},\ X = \frac{x}{x_{PC}},\ H = \frac{q_r}{4\sigma T_0^4},$$

$$\theta_g = \frac{T_g}{T_0},\ \theta_s = \frac{T_s}{T_0},\ S = \frac{ut}{x_{PC}},\ RR = \frac{Rs.Pr.w}{Re_{PC}},\ Ka = \frac{\alpha U_w}{h_v},\ J = \frac{\pi I}{\sigma T_s^4}$$

5.2.1 Dimensionless form of governing equation

Using dimensionless parameter, the governing equations in FP section, $-x_{FP} \le x \le -L \ \left(\tau_{-x_{FP}} \le \tau \le \tau_{-L}\right)$ are normalized. The dimensionless energy equation of solid is given

$$(1-\varepsilon)\Gamma\frac{\partial\theta_s}{\partial S}=\left(\frac{CD}{Re_{FP}\,Pr}\right).\left(\frac{\partial^2\theta_s}{\partial X^2}\right)-\left(\frac{\tau_{FP}^2}{Re_{FP}\,Pr\,Nr}\right).\left(\frac{\partial H}{\partial\tau}\right)-\left(\frac{Mp}{Re_{FP}\,Pr}\right)(\theta_s-\theta_F).$$

(5.21)

Where the dimensionless local net radiative heat flux within the FP is expressed as:

$$H_r^{\,n}(\tau)=H_r^{\,+}(\tau)+H_r^{\,-}(\tau),$$

$$H_r^{\,+}(\tau)=\frac{1}{2}\left[J_0^{+}(\tau_{-x_{FP}})E_3\left(\tau_{-x_{FP}}-\tau\right)+\int_{\tau_{-x_{FP}}}^{\tau}\theta_s^4(\tau')E_2(\tau'-\tau)\,d\tau\right],\qquad \text{and} \qquad (5.22)$$

$$H_r^{\,-}(\tau)=-\frac{1}{2}\left[J_0^{-}(\tau_{x_{PC}})E_3\left(\tau_{x_{PC}}\right)+\int_{0}^{\tau_{x_{PC}}}\theta_s^4(\tau')E_2(\tau')\,d\tau'\right]E_3(\tau)$$
$$-\frac{1}{2}\left[\int_{\tau}^{\tau_{-L}}\theta_s^4(\tau')E_2(\tau-\tau')\,d\tau'\right]. \qquad (5.23)$$

The divergence of the dimensionless net radiative heat flux is expressed as:

$$\frac{\partial H_r^{n}(\tau)}{\partial\tau}=-\frac{1}{2}\left[-2J_b(\tau)+\int_{\tau_{-x_{FP}}}^{\tau_{-L}}\theta_s^4(\tau')E_1\left(|\tau-\tau'|\right)d\tau'+J_0^{+}\left(\tau_{-x_{FP}}\right)E_2\left(\tau_{-x_{FP}}-\tau\right)\right]$$
$$-\frac{1}{2}\left[J_0^{-}\left(\tau_{x_{PC}}\right)E_3\left(\tau_{x_{PC}}\right)+\int_{0}^{\tau_{x_{PC}}}\theta_s^4(\tau')E_2(\tau')\,d\tau'\right]E_2(\tau)$$
$$-\frac{1}{2}\left[J_0^{-}\left(\tau_{x_{PC}}\right)E_2\left(\tau_{x_{PC}}\right)+J_b(\tau')+\int_{0}^{\tau_{x_{PC}}}\theta_s^4(\tau')E_1(\tau')\,d\tau'\right]E_3(\tau).$$

(5.24)

The energy equation of fluid phase in dimensionless form is expressed as

$$\varepsilon\frac{\partial\theta_F}{\partial S}+\varepsilon\frac{\partial\theta_F}{\partial X}=\left(\frac{\varepsilon}{Re_{FP}\,Pr}\right)\frac{\partial^2\theta_F}{\partial X^2}+\left(\frac{Mp}{Re_{FP}\,Pr}\right)(\theta_s-\theta_F),\ \text{and} \qquad (5.25)$$

The subscript F in equation (5.25) means liquid phase (in liquid preheated zone) and gas phase (in superheated vapor zone).

In small evaporation volume, the dimensionless fluid temperature is expressed as

$$\theta_F = \frac{T_b}{T_0} \tag{5.26}$$

In the PC section, $0 \le x \le x_{PC}$ $\left(\tau_0 \le \tau \le \tau_{x_{PC}}\right)$, the conservation equation for energy of gas phase in PC in dimensionless form is given by

$$\frac{\partial\theta_g}{\partial S} + \frac{\partial\theta_g}{\partial X} = \left(\frac{1}{Re_{x_{PC}}\,Pr}\right)\frac{\partial^2\theta_g}{\partial X^2} + \left(\frac{H_o}{Re_{x_{PC}}\,Pr}\right)RR(i) - \left(\frac{Mp}{\varepsilon\,Re_{x_{PC}}\,Pr}\right)(\theta_g - \theta_s) - \left(\frac{KaMp}{\varepsilon\,Re_{x_{PC}}\,Pr}\right)(\theta_g - \theta_w). \tag{5.27}$$

The dimensionless parameter Ka in the last term of the right-hand side of equation (5.27) is already defined in section 4.2.1.

The dimensionless conservation equation for the species of gas phase in PC is given by

$$\frac{\partial Y}{\partial S} + \frac{\partial Y}{\partial X} = \left(\frac{1}{Re_{PC}\,Le\,Pr}\right)\frac{\partial^2 Y}{\partial X^2} + \left(\frac{1}{Re_{PC}\,Pr}\right)RR(i). \tag{5.28}$$

The conservation equation for the energy of solid phase in PC in dimensionless form is given by

$$\Gamma(1-\varepsilon)\frac{\partial\theta_s}{\partial S} = \left(\frac{CD}{Re_{PC}\,Pr}\right)\frac{\partial^2\theta_s}{\partial x^2} - \left(\frac{\tau_{PC}^2}{Re_{PC}\,Pr\,Nr}\right)\frac{\partial H}{\partial\tau} + \left(\frac{Mp}{Re_{PC}\,Pr}\right)(\theta_g - \theta_s). \tag{5.29}$$

Where the local net radiative heat flux within the PC is expressed as:

$$H_r^{\,n}(\tau) = H_r^{+}(\tau) + H_r^{-}(\tau),$$

$$H_r^+(\tau)=\frac{1}{2}\left[J_0^+(\tau_{-x_{FP}})E_3\left(\tau_{-x_{FP}}\right)+\int_{\tau_{-x_{FP}}}^{\tau_{-L}}\theta_s^4(\tau')E_2(\tau')d\tau'\right]E_3(\tau)$$
$$+\frac{1}{2}\left[\int_0^{\tau}\theta_s^4(\tau')E_2(\tau-\tau')d\tau'\right], \quad (5.30)$$

$$H_r^-(\tau)=-\frac{1}{2}\left[J_0^-(\tau_{x_{PC}})E_3\left(\tau_{x_{PC}}-\tau\right)+\int_{\tau}^{\tau_{x_{PC}}}\theta_s^4(\tau')E_2(\tau'-\tau)d\tau'\right]. \quad (5.31)$$

The dimensionless divergence of the net radiative heat flux, $\frac{\partial H_r^n(\tau)}{\partial\tau}$ is expressed as:

$$\frac{\partial H_r^n(\tau)}{\partial\tau}=-\frac{1}{2}\left[J_0^+\left(\tau_{-x_{FP}}\right)E_3\left(\tau_{-x_{FP}}\right)+\int_{\tau_{-x_{FP}}}^{\tau_{-L}}\theta_s^4(\tau')E_2(\tau')d\tau'\right]E_2(\tau)$$
$$-\frac{1}{2}\left[-2J_b(\tau)+J_0^-\left(\tau_{x_{PC}}\right)E_2\left(\tau_{x_{PC}}-\tau\right)+\int_0^{\tau_{x_{PC}}}\theta_s^4(\tau')E_1\left(|\tau-\tau'|\right)d\tau'\right] \quad (5.32)$$
$$-\frac{1}{2}\left[J_0^+\left(\tau_{-x_{FP}}\right)E_2\left(\tau_{-x_{FP}}\right)+J_b(\tau')+\int_{\tau_{-x_{FP}}}^{\tau_{-L}}\theta_s^4(\tau')E_1(\tau')d\tau'\right]E_3(\tau).$$

Next step, the governing equation of energy and species in dimensionless form both in FP and PC zones are discretized by differential approximations

5.2.2 Differential approximations

The differential approximation method is presented in previous section 4.2.2. The governing equations both in FP and PC are discretized and rearranged. Later the discretized governing equation will be solved by a numerical solution through the iterative process. Simple equation forms are prepared for solving by numerical method through the following.

In FP section, $-x_{FP}\le x\le -L$ $\left(\tau_{-x_{FP}}\le\tau\le\tau_{-L}\right)$

$$\left(\theta_F\right)_i^j = \frac{1}{\left(\frac{1}{\Delta S}+\frac{1}{\Delta X}+\frac{2}{Re_{FP}\,Pr\,\Delta X^2}+\frac{Mp}{\varepsilon\,Re_{FP}\,Pr}\right)}\cdot\left\{\frac{\left(\theta_F\right)_i^{j-1}}{\Delta S}+\frac{\left(\theta_F\right)_{i-1}^{j}}{\Delta X}\right.$$
$$\left.\left(\frac{1}{Re_{FP}\,Pr\,\Delta X^2}\right)\left[\left(\theta_F\right)_{i+1}^{j}+\left(\theta_F\right)_{i-1}^{j}\right]+\left(\frac{Mp}{\varepsilon\,Re_{FP}\,Pr}\right)\left(\theta_s\right)_i^j\right\} \qquad (5.33)$$

$$\left(\theta_s\right)_i^j = \frac{1}{\left(\frac{\Gamma(1-\varepsilon)}{\Delta S}+\frac{2CD}{Re_{FP}\,Pr\,\Delta X^2}+\frac{Mp}{Re_{FP}\,Pr}\right)}\cdot\left\{\left(\frac{\Gamma(1-\varepsilon)}{\Delta S}\right)\left(\theta_s\right)_i^{j-1}+\frac{\left(\theta_F\right)_{i-1}^{j}}{\Delta X}\right.$$
$$\left(\frac{CD}{Re_{FP}\,Pr\,\Delta X^2}\right)\left[\left(\theta_s\right)_{i+1}^{j}+\left(\theta_s\right)_{i-1}^{j}\right]+\left(\frac{Mp}{Re_{FP}\,Pr}\right)\left(\theta_F\right)_i^j \quad .$$
$$\left.-\left(\frac{\tau_{FP}^2}{Re_{FP}\,Pr\,\Delta X^2}\right)\cdot\left(\frac{\partial H}{\partial\tau}\right)\right\} \qquad (5.34)$$

In the PC section, $0 \le x \le x_{PC}$ $\left(\tau_0 \le \tau \le \tau_{x_{PC}}\right)$

$$\left(\theta_g\right)_i^j = \frac{1}{\left(\frac{1}{\Delta S}+\frac{1}{\Delta X}+\frac{2}{Re_{PC}\,Pr\,\Delta X^2}+\frac{Mp}{\varepsilon\,Re_{PC}\,Pr}+\frac{KaMp}{\varepsilon\,Re_{PC}\,Pr}\right)}\cdot\left\{\frac{\left(\theta_g\right)_i^{j-1}}{\Delta S}+\frac{\left(\theta_g\right)_{i-1}^{j}}{\Delta X}\right.$$
$$\left(\frac{1}{Re_{PC}\,Pr\,\Delta X^2}\right)\left[\left(\theta_g\right)_{i+1}^{j}+\left(\theta_g\right)_{i-1}^{j}\right]+\left(\frac{Ho}{Re_{PC}\,Pr}\right)RR_i^j+\left(\frac{Mp}{\varepsilon\,Re_{PC}\,Pr}\right)\left(\theta_s\right)_i^j$$
$$\left.+\left(\frac{KaMp}{\varepsilon\,Re_{PC}\,Pr}\right)\theta_w\right\} \qquad (5.35)$$

$$Y_i^j = \frac{1}{\left(\frac{1}{\Delta S}+\frac{1}{\Delta X}+\frac{2}{Re_{PC}\,Le\,Pr\,\Delta X^2}+ARR_i^j\right)}\cdot\left\{\left(\frac{Y_i^j}{\Delta S}\right)+\frac{Y_{i-1}^j}{\Delta X}\right.$$
$$\left.\left(\frac{1}{Re_{PC}\,Le\,Pr\,\Delta X^2}\right)\left[Y_{i+1}^j+Y_{i-1}^j\right]+ARR_i^j\right\} \qquad (5.36)$$

Where, $$ARR_i^j = \frac{Rs.\exp\left[-E_a/\left(\theta_g\right)_i^j\right]}{Re_{PC}}$$

$$\left(\theta_s\right)_i^j = \frac{1}{\left(\frac{\Gamma\left(1-\varepsilon\right)}{\Delta S} + \frac{2CD}{Re_{PC}\,Pr\,\Delta X^2} + \frac{Mp}{Re_{PC}\,Pr}\right)} \cdot \left\{\left(\frac{\Gamma\left(1-\varepsilon\right)}{\Delta S}\right)\left(\theta_s\right)_i^{j-1} + \frac{\left(\theta_s\right)_{i-1}^j}{\Delta X}\right.$$
$$\left.\left(\frac{CD}{Re_{PC}\,Pr\,\Delta X^2}\right)\left[\left(\theta_s\right)_{i+1}^j + \left(\theta_s\right)_{i-1}^j\right] + \left(\frac{Mp}{Re_{PC}\,Pr}\right)\left(\theta_g\right)_i^j - \left(\frac{\tau_{PC}^2}{Re_{PC}\,Pr\,\Delta X^2}\right)\cdot\left(\frac{\partial H}{\partial \tau}\right)\right\} \tag{5.37}$$

Non-dimensional equations (5.33) - (5.37) are solved numerically along the characteristics. Local and global energy balance equations, which are used to check the accuracy of the model, are given in the following sections.

5.2.3 Non-dimensional energy equations

In FP section, $-x_{FP} \le x \le -L$ $\left(\tau_{-x_{FP}} \le \tau \le \tau_{-L}\right)$

The local energy balance equation for fluid and solid phase via the following,

$$\left(\frac{\varepsilon}{Re_{FP}\,Pr}\right)\frac{\partial^2\theta_F}{\partial X^2} + \left(\frac{Mp}{Re_{FP}\,Pr}\right)\left(\theta_s - \theta_F\right) - \varepsilon\frac{\partial\theta_F}{\partial X} = 0\text{, and} \tag{5.38}$$

$$\left(\frac{CD}{Re_{FP}\,Pr}\right)\cdot\left(\frac{\partial^2\theta_s}{\partial X^2}\right) - \left(\frac{\tau_{FP}^2}{Re_{FP}\,Pr\,Nr}\right)\cdot\left(\frac{\partial H}{\partial \tau}\right) - \left(\frac{Mp}{Re_{FP}\,Pr}\right)\left(\theta_s - \theta_F\right) = 0 \tag{5.39}$$

In the PC section, $0 \le x \le x_{PC}$ $\left(\tau_0 \le \tau \le \tau_{x_{PC}}\right)$

The local energy balance equation for gas and solid phase are list as following,

$$\left(\frac{\varepsilon}{Re_{x_{PC}}\,Pr}\right)\frac{\partial^2\theta_g}{\partial X^2} + \left(\frac{\varepsilon H_o}{Re_{x_{PC}}\,Pr}\right)RR\left(i\right) - \left(\frac{Mp}{Re_{x_{PC}}\,Pr}\right)\left(\theta_g - \theta_s\right)$$
$$-\varepsilon\frac{\partial\theta_g}{\partial X} - \left(\frac{KaMp}{Re_{x_{PC}}\,Pr}\right)\left(\theta_g - \theta_w\right) = 0 \tag{5.40}$$

$$\left(\frac{CD}{Re_{PC}\,Pr}\right)\frac{\partial^2\theta_s}{\partial x^2}-\left(\frac{\tau_{PC}^2}{Re_{PC}\,Pr\,Nr}\right)\frac{\partial H}{\partial\tau}+\left(\frac{Mp}{Re_{PC}\,Pr}\right)(\theta_g-\theta_s)=0\,. \tag{5.41}$$

The global energy balance for the system is expressed

$$\begin{aligned}&\left[\int_1^N\left\{\left(\frac{\varepsilon}{Re_{FP}\,Pr}\right)\frac{\partial^2\theta_F}{\partial X^2}+\cancel{\left(\frac{Mp}{Re_{FP}\,Pr}\right)}(\theta_s-\theta_F)-\varepsilon\frac{\partial\theta_F}{\partial X}\right.\right.\\&\left.\left.+\left(\frac{CD}{Re_{FP}\,Pr}\right)\cdot\left(\frac{\partial^2\theta_s}{\partial X^2}\right)-\left(\frac{\tau_{FP}^2}{Re_{FP}\,Pr\,Nr}\right)\cdot\left(\frac{\partial H}{\partial\tau}\right)-\cancel{\left(\frac{Mp}{Re_{FP}\,Pr}\right)}(\theta_s-\theta_F)\right\}dX\right]_{FP}\\&+\left[\int_1^N\left\{\left(\frac{\varepsilon}{Re_{x_{PC}}\,Pr}\right)\frac{\partial^2\theta_g}{\partial X^2}+\left(\frac{\varepsilon H_o}{Re_{x_{PC}}\,Pr}\right)RR(i)-\cancel{\left(\frac{Mp}{Re_{x_{PC}}\,Pr}\right)}(\theta_g-\theta_s)-\varepsilon\frac{\partial\theta_g}{\partial X}\right.\right.\\&\left.\left.-\left(\frac{KaMp}{Re_{x_{PC}}\,Pr}\right)(\theta_g-\theta_w)+\left(\frac{CD}{Re_{PC}\,Pr}\right)\frac{\partial^2\theta_s}{\partial x^2}-\left(\frac{\tau_{PC}^2}{Re_{PC}\,Pr\,Nr}\right)\frac{\partial H}{\partial\tau}\right.\right.\\&\left.\left.+\cancel{\left(\frac{Mp}{Re_{PC}\,Pr}\right)}(\theta_g-\theta_s)\right\}dX\right]_{PC}=0.\end{aligned} \tag{5.42}$$

The rearrange global energy balance is

$$\begin{aligned}&\left[\int_1^N\left\{\left(\frac{\varepsilon}{Re_{FP}\,Pr}\right)\frac{\partial^2\theta_F}{\partial X^2}-\varepsilon\frac{\partial\theta_F}{\partial X}+\left(\frac{CD}{Re_{FP}\,Pr}\right)\cdot\left(\frac{\partial^2\theta_s}{\partial X^2}\right)\right.\right.\\&\left.\left.-\left(\frac{\tau_{FP}^2}{Re_{FP}\,Pr\,Nr}\right)\cdot\left(\frac{\partial H}{\partial\tau}\right)\right\}dX\right]_{FP}\\&+\left[\int_1^N\left\{\left(\frac{\varepsilon}{Re_{x_{PC}}\,Pr}\right)\frac{\partial^2\theta_g}{\partial X^2}+\left(\frac{\varepsilon H_o}{Re_{x_{PC}}\,Pr}\right)RR(i)-\varepsilon\frac{\partial\theta_g}{\partial X}-\left(\frac{KaMp}{Re_{x_{PC}}\,Pr}\right)(\theta_g-\theta_w)\right.\right.\\&\left.\left.+\left(\frac{CD}{Re_{PC}\,Pr}\right)\frac{\partial^2\theta_s}{\partial x^2}-\left(\frac{\tau_{PC}^2}{Re_{PC}\,Pr\,Nr}\right)\frac{\partial H}{\partial\tau}\right\}dX\right]_{PC}=0.\end{aligned} \tag{5.43}$$

Later the problem will be solved by the Newton-Raphson's iteration method, which will be explained the solving process will show in Appendix A. The measured temperature is used as an initial guess at first. Then the computing step by step is done until the answer can be accepted by convergence criteria.

5.3 Results and discussion

5.3.1 Model validation

Fig.5.3 shows calculated temperature profiles of liquid, gas and solid for firing rate, FR of 5.74 kW and equivalence ratio Φ = 0.64. When the combustion occurs in PC, radiation heat is emitted from PC to FP. Thus, T_s are greater than T_F for all of location in FP. Then the liquid fuel flows into FP, the liquid fuel is preheated in $-95 \le x \le -62$. When T_F reach T_b, the liquid fuel is evaporated and changed to gas phase at the evaporation front (x = -61.25). The gas fuel is preheated in $-60.5 \le x \le -20$, and the superheated vapor flow out at x = -20. Owing to the porous FP have the high surface to volume ratio (1.23×10^4 m^2/m^3) lead to high heat transfer between fluid and solid phase. Thus, fluid and solid temperature are almost equal. The result implies that the evaporation front in FP with solid temperature. At the pre-flame zone in PC $(0 \le x \le 12)$, T_s is higher than T_g, thus heat is transferred from solid to gas. On the other hand, at the post-flame zone in PC $(12 \le x \le 160)$, where the gas is hotter than the solid, the gas phase transfers heat to the solid phase. Simultaneously, the solid matrix is recirculate heat from the post-flame zone to the pre-flame zone by solid to solid with conduction and radiation. Thus, T_g decreases before pass through the system. Hence, the higher peak temperature of gas phase compare with the adiabatic flame temperature (at the initial temperature of reactant is ambient temperature) due to internal heat recirculation. Wall temperature of 1237 ^oC is predicted, yielding preheated air temperature of T_{ao} = 160 ^oC before mixing with the fuel followed by the combustion in the PC. Moreover, the numerical results yield the same trends as those of the experimental ones. At the downstream zone of PC, the predicted T_s is higher than the measured T_{exp} because heat is lost to the surroundings. The results confirmed that the numerical model with assumptions of infinitely fast mixing and one-step global irreversible reaction can be used to predict the non-premixed porous burner. In addition, the isothermal thin film flash evaporation model is reasonable to predict NSPB.

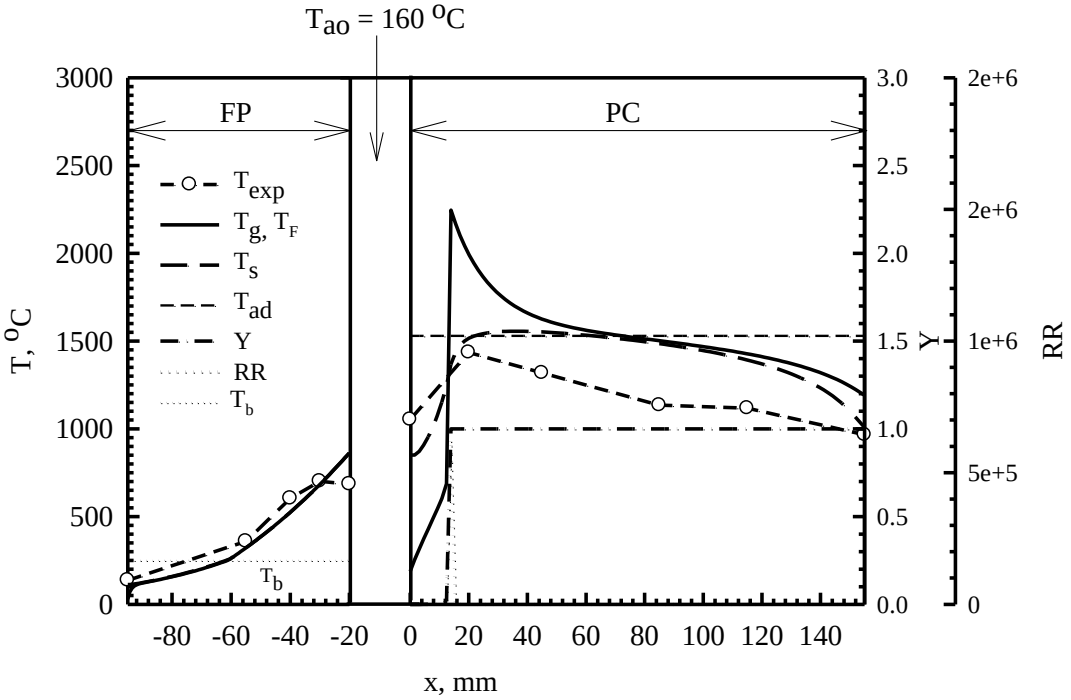

Figure 5.3 The comparison between predicted and measured temperature profiles at 5.74 kW and Φ = 0.64.

5.3.2 Local energy balance

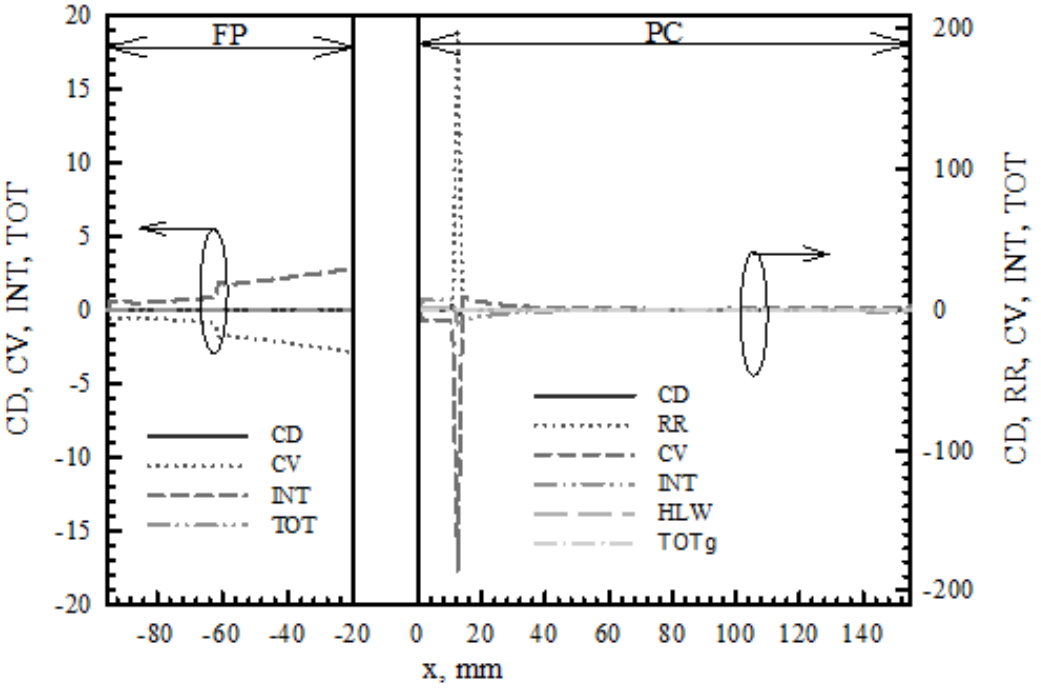

Figure 5.4 Local energy balance of fluid-phase at 5.74 kW and Φ = 0.64.

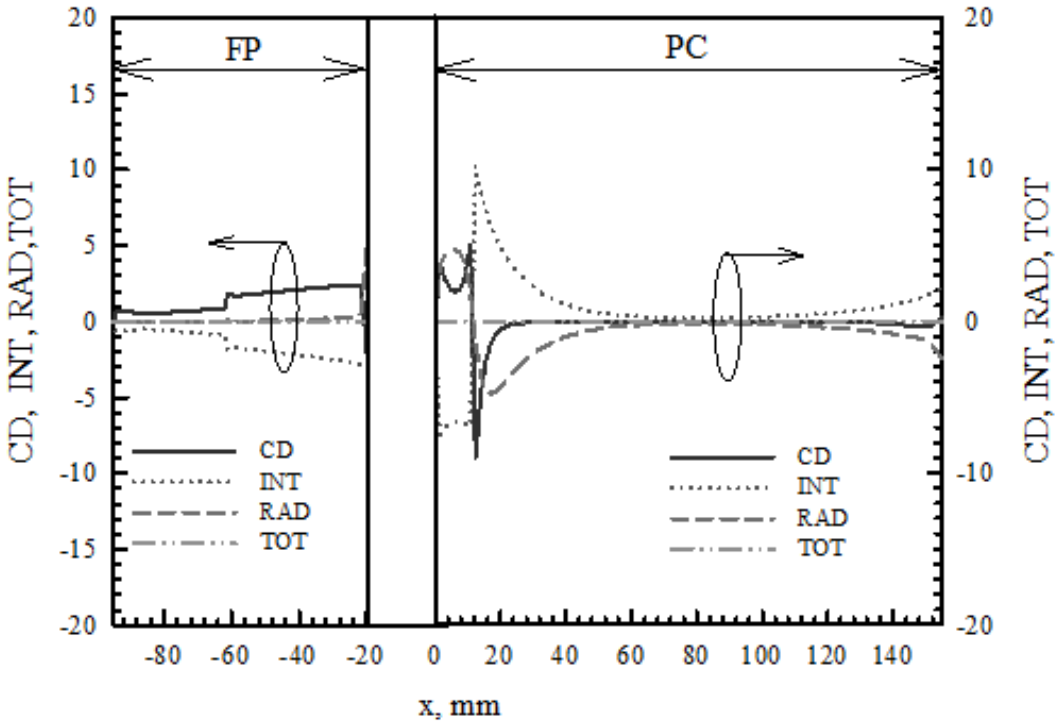

Figure 5.5 Local energy balance of solid-phase at 5.74 kW and Φ = 0.64.

The local energy balance of fluid phase at FR = 5.74 kW and Φ = 0.64. CD, RR,CV, INT, and TOT represent the dimensionless fluid phase heat conduction, combustion heat release rate, convection, heat transfer between the fluid and solid phase and local total energy, respectively as shown in Fig. 5.4. Considering in FP, at $-95 \le x \le -61.25$, the fuel is in liquid phase; and after x = -61.25, the fuel is in gas phase. CV mainly balances with INT and the positive INT represent heat transferred from the solid to the gas. At evaporation front (x = -61.25), the CV and INT are significantly increased due to phase change cause to higher density and flow velocity. In PC, at the reaction zone, RR mainly balances with CV. At the pre-flame and post flame zones CV mainly balance with INT. HLW has negative sign all position, which represent heat lost from the hot gas to the wall. Furthermore, the positive INT represent heat transferred from solid to gas phase for preheated mixture before entering into reaction zone at the pre-flame zone. On the other hand, in the post-flame zone, the INT is negative; mean heat is transferred from the hot product to the solid matrix before flowing out from PC.

Fig. 5.5 shows the local energy balance of solid phase at FR = 5.74 kW and Φ = 0.64. CD, INT, RAD, and TOT are the dimensionless solid phase heat conduction, heat transfer between the phase, solid radiation and local total energy, respectively. Almost all of location in FP, INT mainly balances with RAD. Except at the downstream of FP; the CD is more important because of the high temperature different at the end of FP (Fig. 5.3). Almost all of locations in PC, INT balance with RAD. At around the reaction zone, CD and RAD are mainly balanced with INT; and at downstream of PC, CD and INT are mainly balanced with RAD. Moreover, the sign of INT is opposite to the INT of gas phase. The total energy balance for fluid and solid phase (TOT) for all of location both in FP and PC are alomost zero. Thus, the global energy balance is 0.2470737%.

5.3.3 Radiative heat flux and divergence of net radiative heat flux

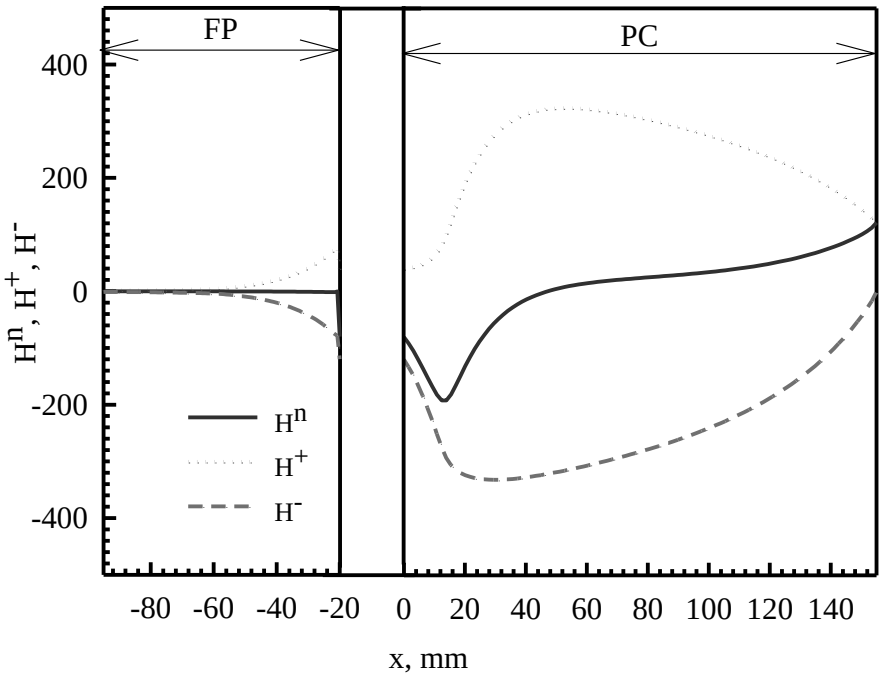

Figure 5.6 Radiative heat flux at 5.74 kW and Φ = 0.64.

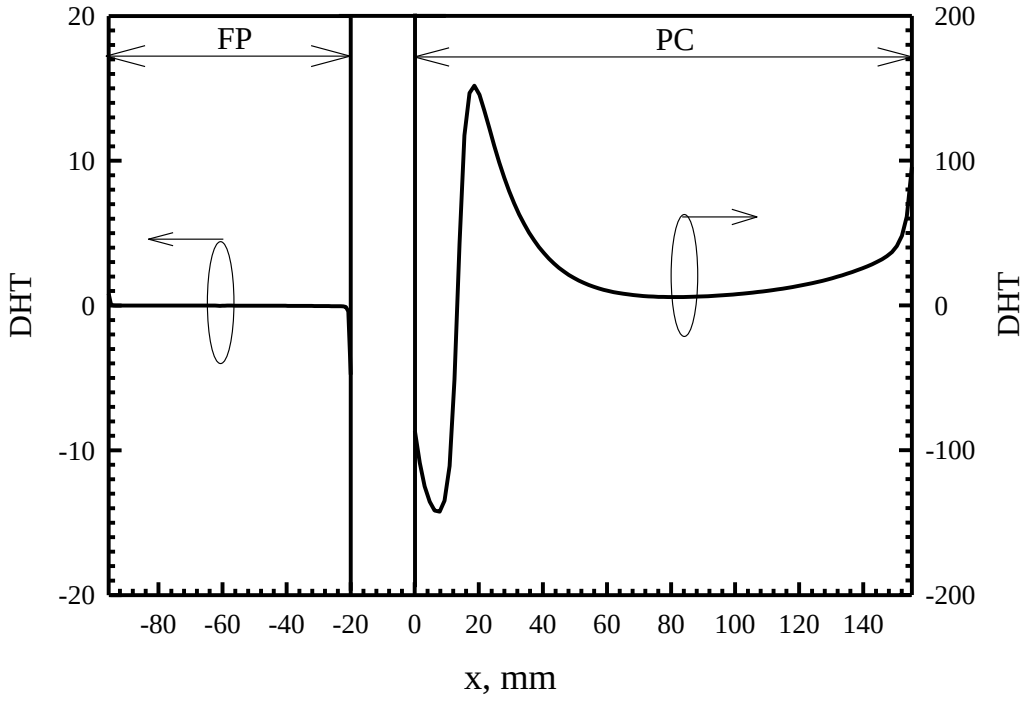

Figure 5.7 Divergence of net radiative heat flux at 5.74 kW and Φ = 0.64.

Fig. 5.6 shows the radiative heat flux in case of non-preheated air at 5.74 kW and Φ = 0.64. The H^+ and H^- mean radiative heat flux, which direction from left to right, and right to left respectively. The H^n mean the net radiative heat flux, which is summation of H^+ and H^-. The pre-flame zone heat is radiated from the reaction zone to the upstream end and then heat is radiated from porous PC to FP (negative H^n) in PC. In FP, heat is radiated from the hot zone (downstream zone) to the cooler zone (upstream zone), thus the H^n is negative near the end of downstream. While at the post-flame zone of PC, heat is radiated from the reaction zone to the downstream zone (positive H^n).

The divergence of net radiative heat flux is shown in Figure 5.7, DHT at 5.74 kW and Φ = 0.64. The negative and positive values of DHT mean the porous is absorber and emitter respectively. At the pre-flame zone of PC, the solid matrix absorbs heat from the flame zone, while heat is transferred convectively from the hot gas to the solid matrix at the post-flame zone of PC. Immediately, the solid

matrix emits heat to the upstream and downstream zone of porous PC. In FP for all of location, the solid matrix is absorber.

5.3.4 Effect of Φ

Fig.5.8 and Fig.5.9 show the effect of Φ for FR of 5.74 kW on the predicted fluid (T_F, T_g) and solid temperature (T_s) respectively. The equivalence ratio (Φ) indicates the quality of mixture and strongly affects the flame temperature. In this study, Φ is increased by decreasing the air flow rate with a fixed FR. The PC and FP temperatures are increased with higher Φ. The reaction zone, is shifted toward the upstream zone of PC with an increasing Φ (Fig.5.8), On the other hand the higher Φ do not significantly affects on evaporation front in FP. Thus, the fuel mass flow rate does not change with higher Φ. In addition, T_s in FP and PC are increased with higher Φ (see Fig.5.9).

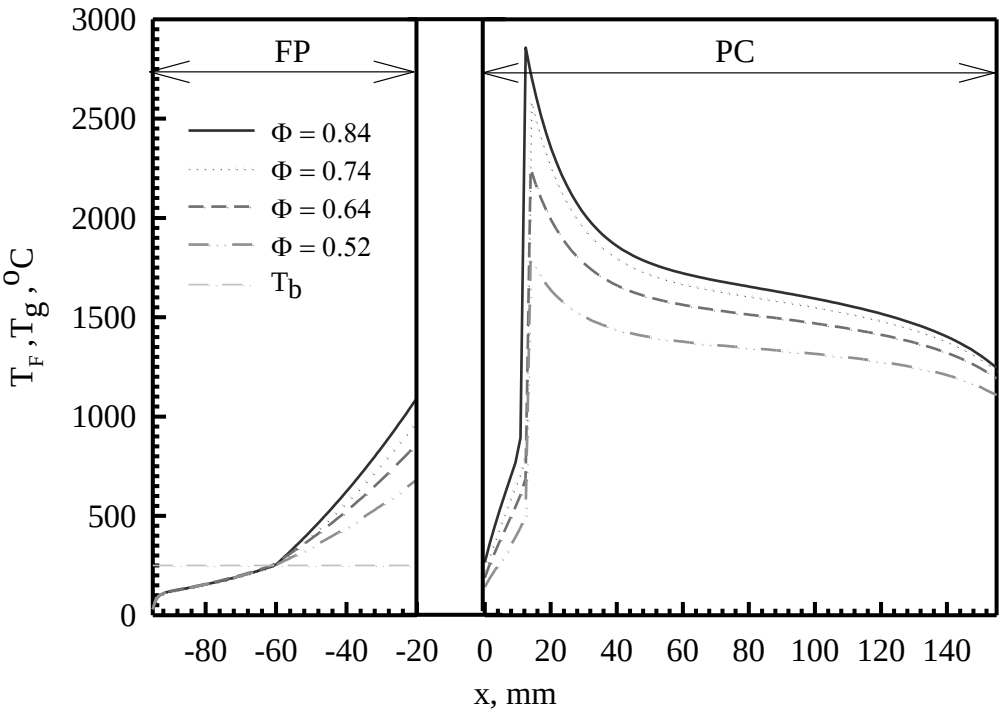

Figure 5.8 Effect of Φ on predicted gas and liquid temperature profiles at 5.74 kW.

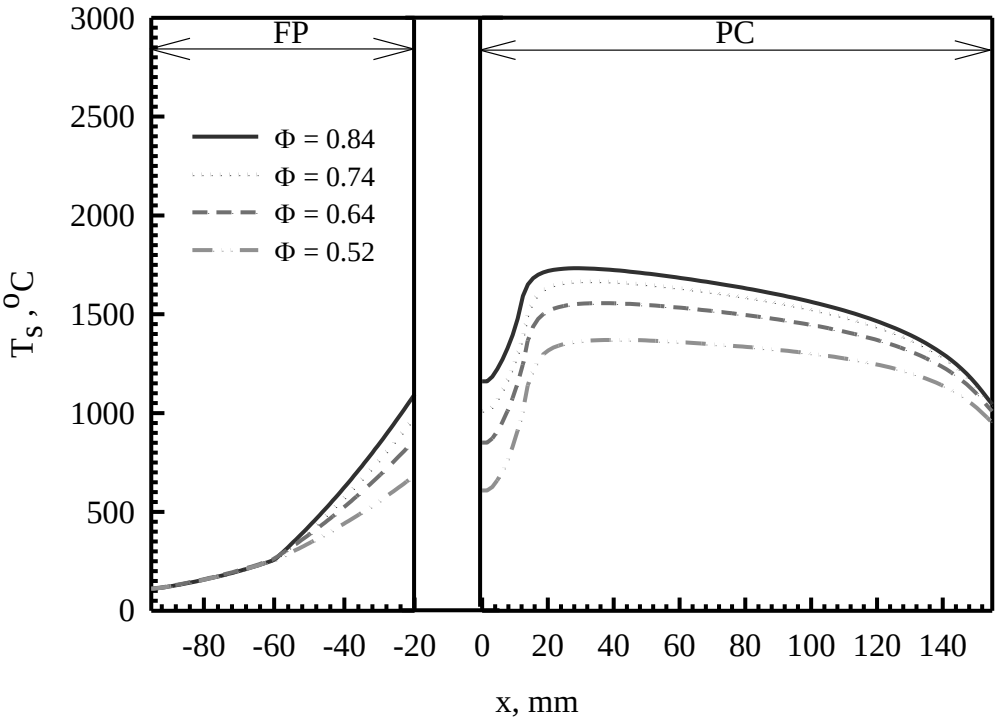

Figure 5.9 Effect of Φ on predicted solid temperature profiles at 5.74 kW.

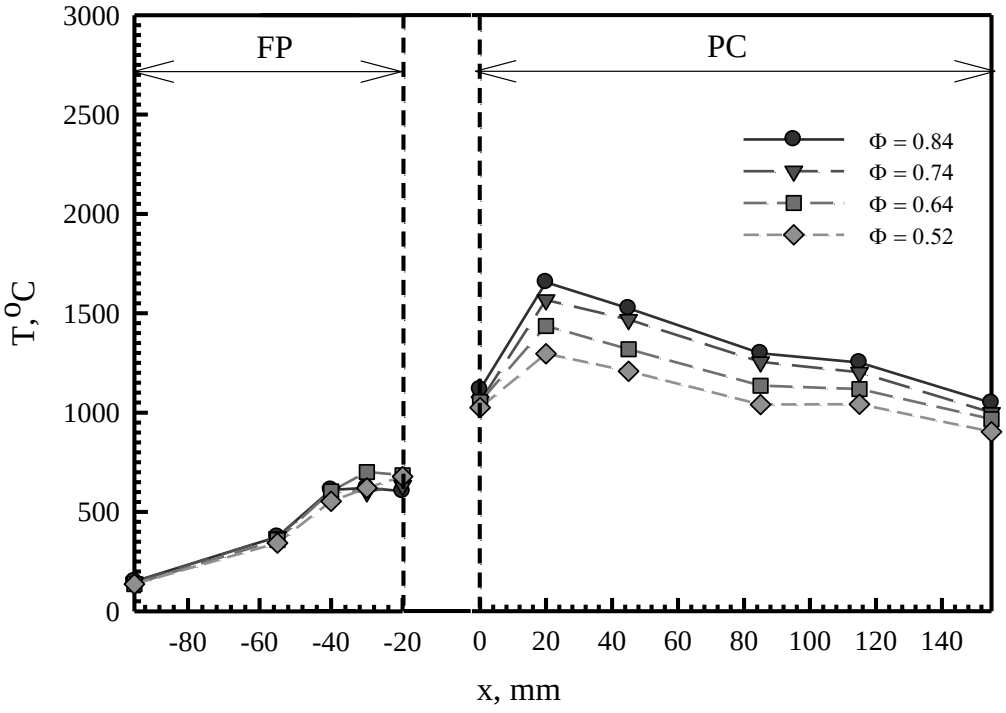

Figure 5.10 Effect of FR on predicted solid temperature profiles at Φ = 0.64.

Fig. 5.10 shows the corresponding measured solid temperature profiles with varying Φ of NSPB. With an increasing Φ, the measured temperature in PC is increased, displaying the same trend as obtained by the model (Fig.5.9). Nevertheless, the measured T in FP does not significantly change with Φ. This may be attributed to a discrepancy between the evaporation model and the actual one, which is a complex phenomenon. The model considers a steady-state condition with a stationary evaporation front, and the evaporation occurs only in a small volume at a temperature of 250 ^{o}C. However, an actual evaporation region is very unstable and liquid kerosene cannot be evaporated in a small volume. Besides, kerosene is a mixture of carbon chains that typically contain between 6 and 16 carbon atoms per molecule. Thus, the boiling temperature of kerosene is between 150 ^{o}C and 275 ^{o}C, and the evaporation zone is wider than that considered in the numerical result. Moreover, it seems that a two-phase region of liquid and vapor of kerosene occurs in this experimental, while the model does not consider these phenomena. However, the predicted temperature profiles (Fig. 5.9) are always in qualitative agreement with the experimental ones, as shown in Fig. 5.10.

5.3.5 Effect of firing rate (FR)

Fig.5.11 shows the effect of FR in the range of 3 – 20 kW on the predicted fuel temperature in FP (T_F) and gas temperature in PC (T_g) at constant Φ = 0.64. In this study, FR is increased with increasing both air and fuel flow rate at fixed Φ. In PC, the temperatures at the post flame zone are increased, but the peak temperatures are decreased with increasing FR. This is due to higher FR followed by higher flow velocity and higher convection heat transfer from the reaction zone to the post flame zone. In FP, increasing FR, the fuel temperatures are decreased, while evaporation fronts significantly move to the downstream zone as magnified in Fig.5.12, because of increasing fuel mass flow rate. In addition, increasing FR result to decreasing T_s in FP, but increasing T_s in PC (Fig.5.13). At FR over than 20 kW, the complete evaporation of fuel within a small volume is not possible. On the other hand, the fuel needs more distance for evaporation, which is a limitation of this model. Thus, for the future work, in order to reach practical, the various boiling temperature of complex hydrocarbon compositions of kerosene should be considered.

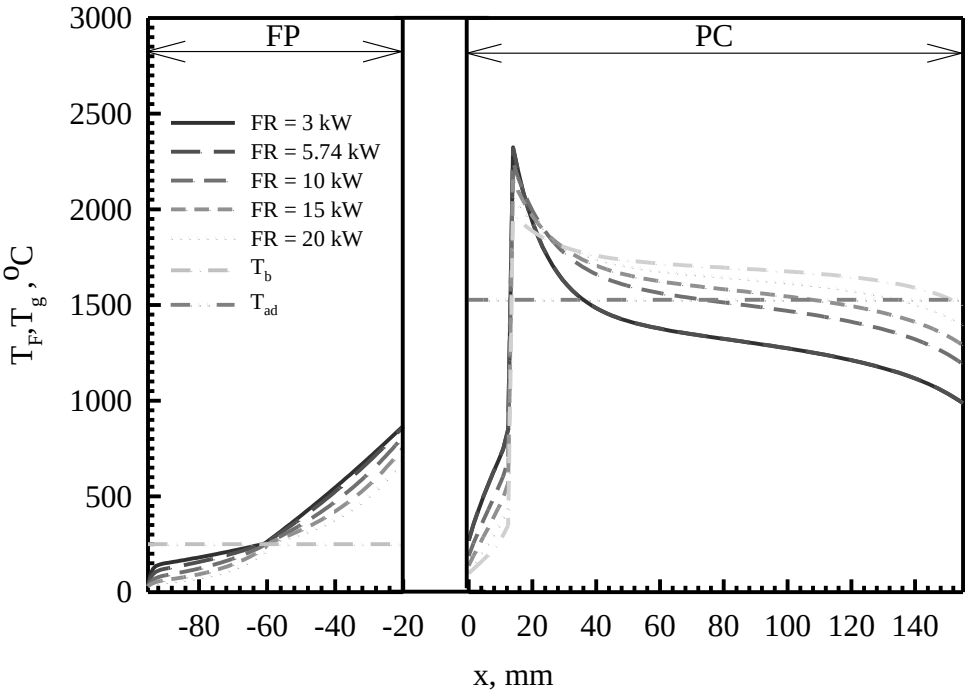

Figure 5.11 Effect of FR on predicted gas and liquid temperature profiles at $\Phi = 0.64$.

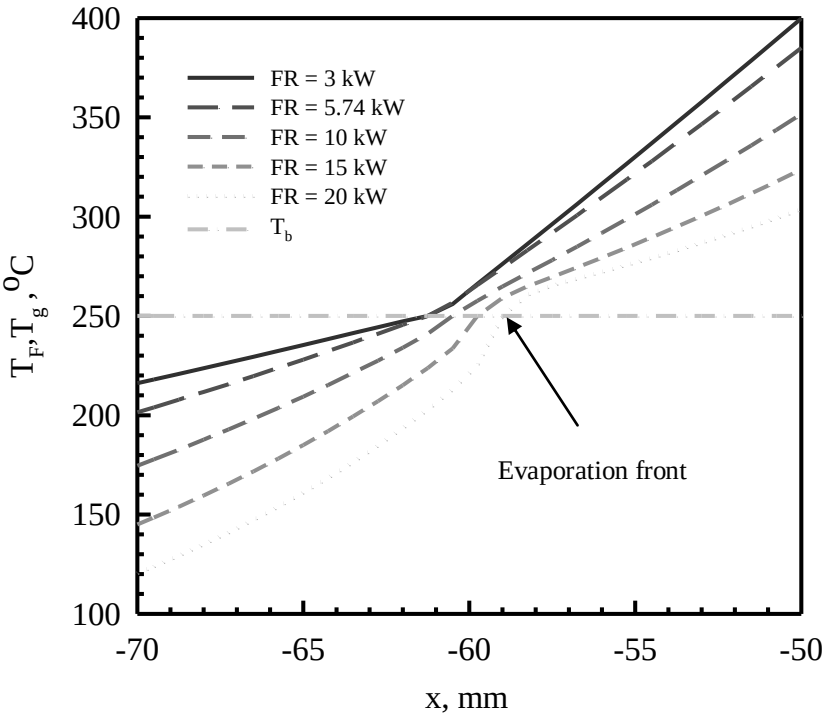

Figure 5.12 Effect of FR on evaporation fronts in FP.

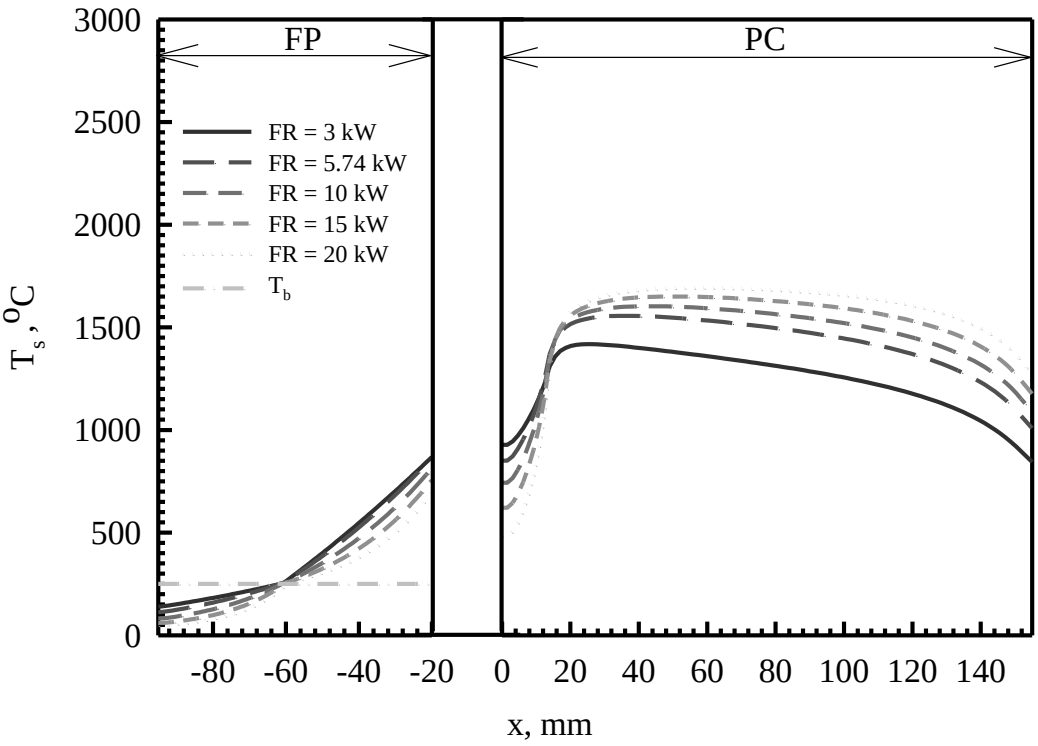

Figure 5.13 Effect of FR on predicted solid temperature profiles at Φ = 0.64.

5.3.6 Burner performance

Radiant output efficiency is an important thermal performance parameter, which indicates the useful energy for heating the product at downstream. The radiant output efficiency can be determined using the following,

$$\eta_{rad} = \frac{\text{heat radiates out the exit of the burner}}{FR}. \tag{5.44}$$

The fuel preheated radiant efficiency is an indicator for quantifying an amount of net radiative heated from the porous PC to the porous FP can be defined as

$$\eta_{pre} = \frac{\text{net heat radiates into FP}}{FR} \tag{5.45}$$

The predicted η_{rad} and η_{pre} are calculated from solid temperature profiles whereas, the measured η_{rad} and η_{pre} are calculated from the measured temperatures via thermocouples, which represent the solid phase temperature.

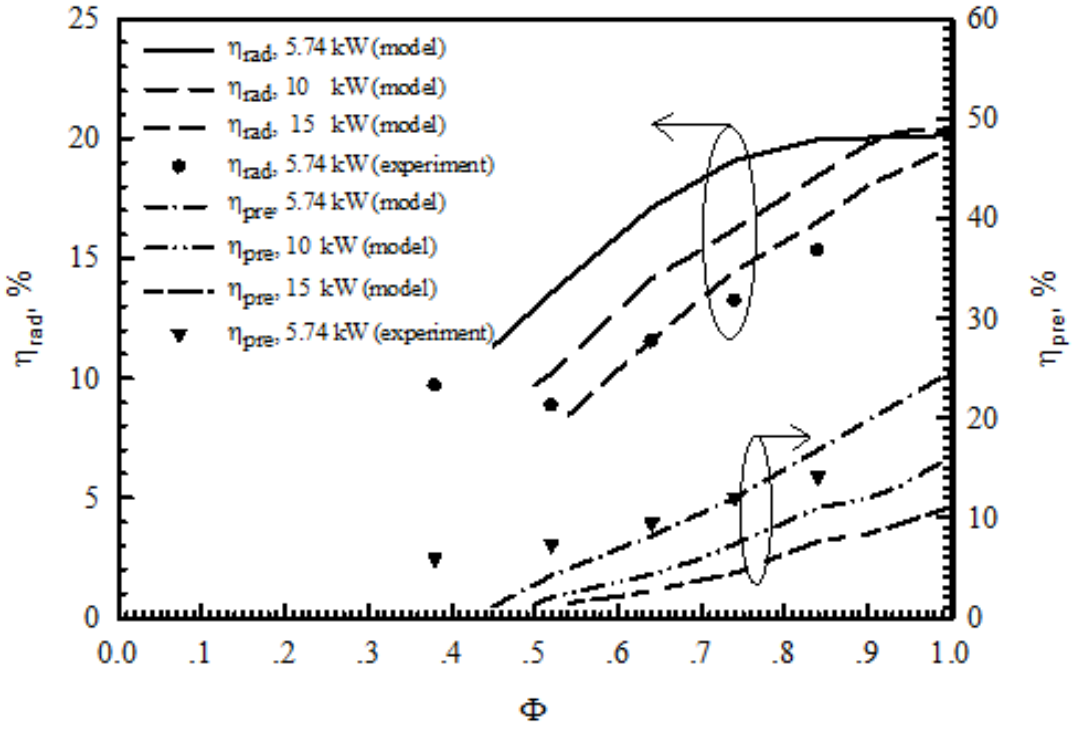

Figure 5.14 η_{rad} as a function of Φ at various FR.

Fig.5.14 shows an effect of Φ on the predicted η_{rad} and η_{pre} at various firing rates, FR. At a constant of Φ, η_{rad} and η_{pre} are decreased with increasing FR. This may be attributed to a large convective loss with a relatively high flow velocity. At a constant FR, η_{rad} is increased Φ because of the higher temperature in PC. Additionally, the flame movement to the upstream zone of PC (see Fig.5.8) is also responsible for an increasing in η_{pre}. The results can be indicated that the temperature at downstream of PC strongly affect η_{rad}, while η_{pre} strongly which depend on the flame location. In addition, the graph shows a comparison of η_{rad} and η_{pre} between numerical results and experimental one at 5.74 kW. The η_{rad} prediction is higher than measured η_{rad} , because the heat lost to the surroundings for experiment. Thus, the predicted temperature and η_{rad} are higher than measured

temperature and η_{rad}. While predicted and measured flame locations are nearby, cause to the predicted and measured η_{pre} has no significant difference. Beside the radiant output efficiency is reported in the range of 8.46-20.38%, which is in the same range as normal premixed porous burner as well as in previous work (e.g. Kayal and Chakravarty, 2006, and Barra and Ellzey, 2004). In previous publications on premixed porous burner shows that the radiant efficiencies were reported cover a wide range of values up to 40% because the differences in the burner design, operating condition and the lack of standard procedure for measuring (Wood and Harris, 2008). In addition, the measured NO_x and CO was reported in the range of 125-190 ppm and 160-220 ppm (by 0% O_2), respectively. The results show that NSPB can be offered higher radiant output efficiency with lower emission compare with conventional spray burner system.

5.3.7 Effect of porous combustor type

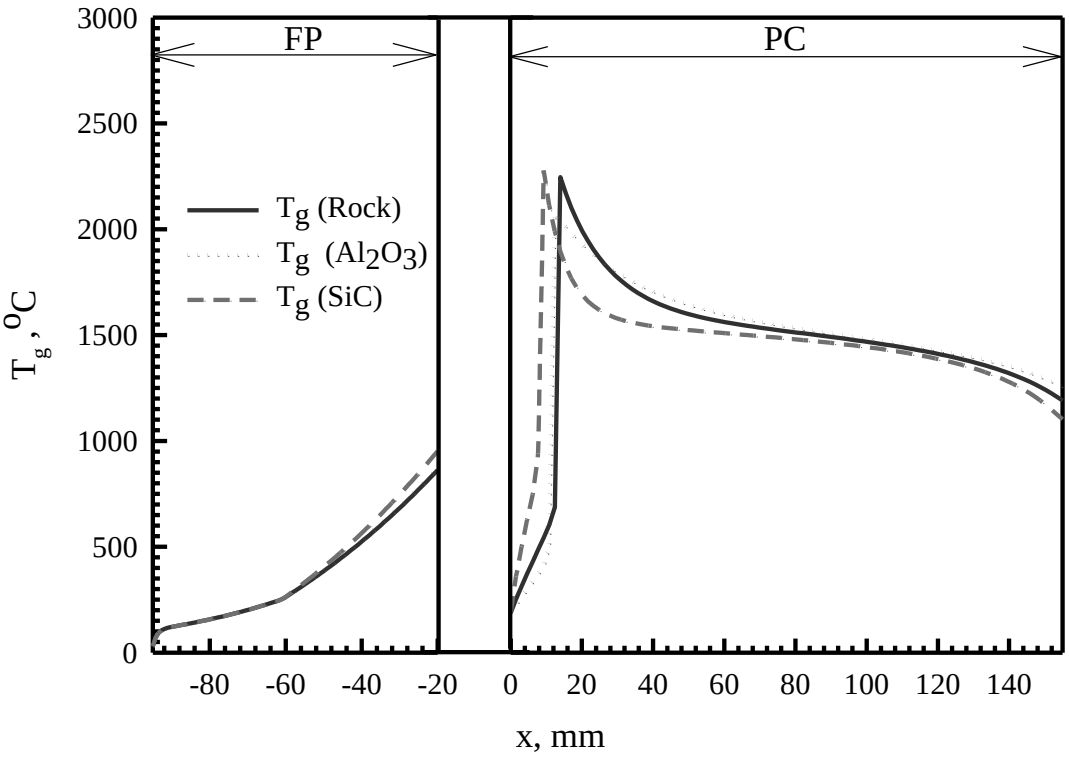

Figure 5.15 Effect of porous material on predicted liquid and gas temperature profiles at FR = 5.74 and Φ = 0.6.

The effect of porous type using in PC is reported in this section. The three type of porous medium: packed bed of rock, fiber lamellae of Al_2O_3 and SiC foam are investigated. The physical properties of porous are already presented in section 4.8. The effect of porous material using in PC on predicted gas and solid temperature (Fig. 5.15 and Fig.5.16). The results shows that porous type have no significantly affect on gas and solid temperature. It can be pointed out that the radiant output efficiency does not change with porous types as shown in Fig.5.17.

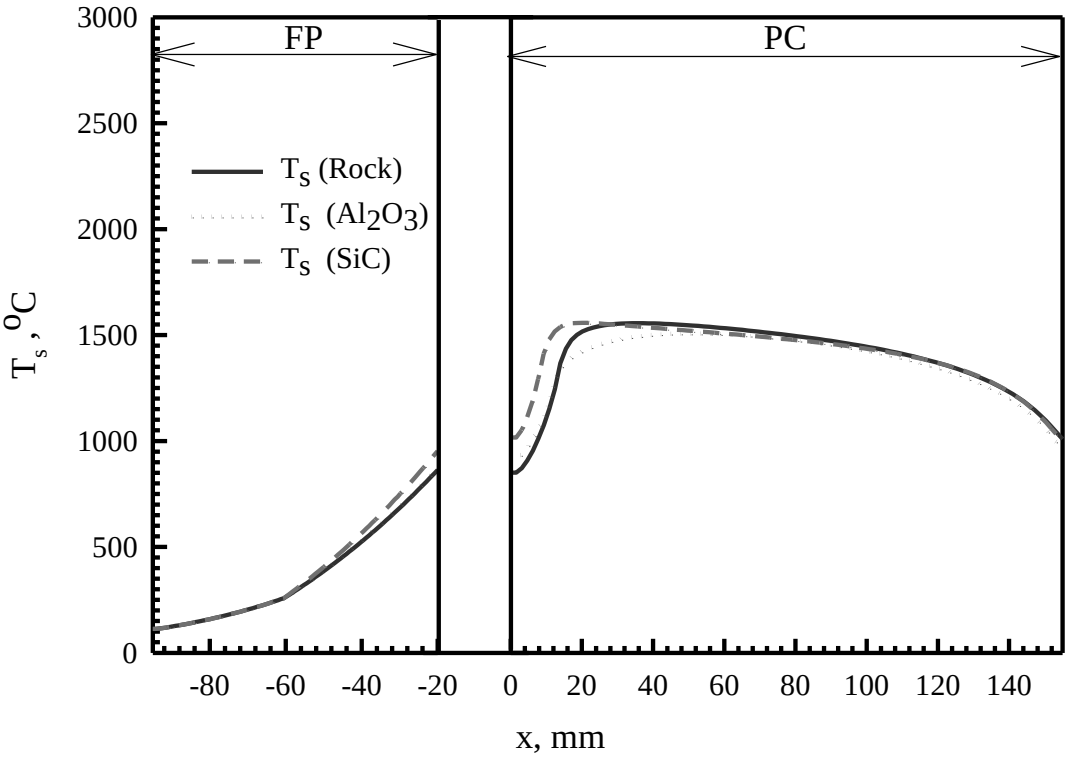

Figure 5.16 Effect of porous material on predicted solid temperature profiles at FR = 5.74 and Φ = 0.6.

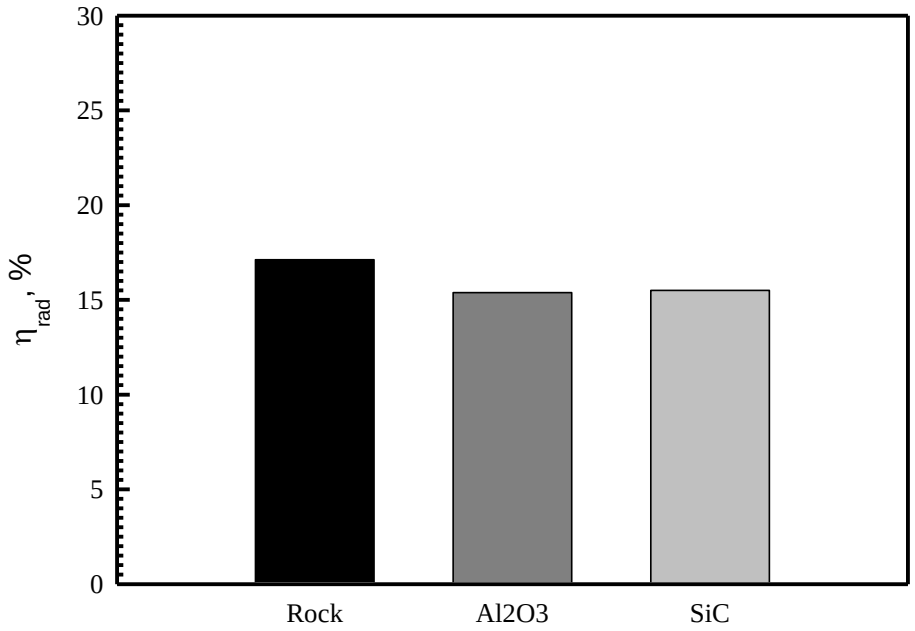

Figure 5.17 Effect of porous material on η_{rad} at FR = 5.74 and Φ = 0.6.

5.4 Conclusions

This chapter presents the non-premixed combustion of liquid kerosene within the porous burner without using atomizer by numerical modeling. The numerical model solves liquid, gas and solid phase energy equation for analyzing evaporation and combustion process. A one-dimension, single-step global reaction model and steady state approach are also considered. The influence of heat transfer between fluid and solid phase, fluid and solid conduction, and solid radiation are also considered. The major conclusions are as follows:

1. The numerical showed similar trends to the experimental. Therefore, the numerical modeling can be used to predict necessary information for burner design.

2. Equivalence ratio (Φ) and firing rate (FR) have significantly affect thermal performance of the NSPB. In additions, η_{rad} and η_{pre} are increased at higher Φ and lower FR.

3. The NSPB is one of alternative technologies, which will be able to replace a conventional sprayed burner by reason of many benefit compare with conventional

sprayed burner. First of all, the complexity of the liquid fuel atomization is eliminated using porous evaporator (FP). Secondly is that the homogeneous combustion within the PC is instead of a heterogeneous combustion in a free space. The last is the NSPB can be designed more compact than the conventional sprayed burner due to the volume to support spray distribution is undesirable. Furthermore, the NSPB provide the high η_{rad} in the same range of conventional premixed porous burner with low emission.